nature communications

Article

https://doi.org/10.1038/s41467-024-50939-0

Hyperbolic-to-hyperbolic transition at exceptional Reststrahlen point in rare-earth oxyorthosilicates

Received: 14 February 2024

Accepted: 25 July 2024

Published online: 15 August 2024

Check for updates

Chunqi Zheng[1,2,3,8], Guangwei Hu[4,8], Jingxuan Wei[1,5], Xuezhi Ma[3], Zhipeng Li[3], Yinzhu Chen[1,6], Zhenhua Ni[6], Peining Li[7], Qian Wang[3] ✉ & Cheng-Wei Qiu[1,2] ✉

Anisotropic optical crystals can exhibit a hyperbolic response within the Reststrahlen band (RB) and support directional polaritonic propagations when interacting with light. Most of the reported low-symmetry optical crystals showcase the evolution from hyperbolic to elliptic dispersion topologies, largely owing to their adjacent RBs being either overlapped or separated. Here, we report an exceptional Reststrahlen point (ERP) in rare-earth oxyorthosilicate Y_2SiO_5, at which two neighboring RBs almost kiss each other. Consequently, we observe the direct hyperbolic-to-hyperbolic topological transition: the hyperbolic branches close and reopen along with the rotating transverse axis (TA). At such ERP, the TA merges to the direction orthogonal to its proximate phonon mode, mainly due to the interplay between these two non-orthogonal phonon modes. We also find that even with the existence of only one single RB, the TA can rotate in-plane. Our findings are prevalent in isostructural rare-earth oxyorthosilicates, such as Lu_2SiO_5. The universally underlying physics of ERP and its corresponding special class of rare-earth oxyorthosilicates may offer playgrounds for continuously tuning phonon polariton propagation direction, and broadband controlling light dispersion of polaritonic nanodevices.

Optical responses in anisotropic mediums are sensitive to polarizations of the incident light, showing non-spherical isofrequency contours (IFCs) in the momentum space. Under extremely anisotropic conditions, the signs of the permittivity along different directions are opposite, leading to hyperbolic response and unbounded IFCs[1–5]. Therein, light can only propagate along the directions between the asymptotes of the IFCs and is forbidden along the perpendicular direction of TA. Thanks to the advancement of nanofabrication, such exotic hyperbolic responses can be realized in many artificial geometries by restricting the moving directions of free electrons, such as alternatively stacked dielectric and metal layers[6–9], fishnet-like structures[10], arrays of nanorod and nanopyramids[11–14]. Also, two-dimensional hyperbolic metasurfaces are proposed, including silver gratings[15], graphene nanoribbons[16–18], and laterally structured

[1]Department of Electrical and Computer Engineering, National University of Singapore, Singapore, Singapore. [2]NUS Graduate School, National University of Singapore, Singapore, Singapore. [3]Institute of Materials Research and Engineering, Agency for Science, Technology and Research (A*STAR), Singapore, Singapore. [4]School of Electrical and Electronic Engineering, Nanyang Technological University, Singapore, Singapore. [5]School of Optoelectronic Science and Engineering, University of Electronic Science and Technology of China, Chengdu, China. [6]Key Laboratory of Quantum Materials and Devices of Ministry of Education, School of Physics, Southeast University, Nanjing, China. [7]Wuhan National Laboratory for Optoelectronics and School of Optical and Electronic Information, Huazhong University of Science and Technology, Wuhan, China. [8]These authors contributed equally: Chunqi Zheng, Guangwei Hu. ✉e-mail: wangqian@imre.a-star.edu.sg; chengwei.qiu@nus.edu.sg

hexagonal boron nitride (hBN)[19,20], which could be characterized using the in-plane conductivity tensor.

Recently, the focus on hyperbolic materials has shifted toward natural materials due to their exemption from complex fabrication. Materials that have been studied range from planar surfaces or slabs, including hBN[21,22], α-MoO_3[23–25], α-V_2O_5[26], black phosphorus[27,28], and WTe_2[29] to bulk crystals such as calcite[30,31], β-Ga_2O_3[32,33], and $CdWO_4$[34]. Based on these natural hyperbolic materials, numerous glamorous physical phenomena have been demonstrated, such as directional energy flow[35], photonic topological transitions[36], ghost surface polaritons[30], planar focusing with curved-edge antenna[37,38], in-plane negative reflection and refraction[39], spin-orbit-locked vortices[40], to name a few.

Lattice symmetry is important to the polaritonic properties of optical crystals. Most studied natural hyperbolic materials such as orthorhombic (e.g., α-MoO_3), hexagonal (e.g., hBN), and trigonal (e.g., calcite) crystals belong to the higher symmetry classes, in which the phonon modes are either parallel or orthogonal to each other. Therefore, the TA of the hyperbolic dispersion curves remains fixed upon changing the working frequency. Lately, phonon polaritons (PhPs) in low-symmetry crystals (LSCs) have aroused extensive attention. Shear polaritons in monoclinic crystals were studied both from far- and near-field, unveiling non-symmetrical response and tilted wavefronts[32–34]. In low-symmetry monoclinic crystals, the RB is bounded between the transverse optic (TO) and longitudinal optic (LO) frequencies. If we define the permittivity along two vertical directions in the **a**–**c** plane as ε_1 and ε_2, two adjacent RBs can be labeled where the real part of ε_a ($a = 1, 2$) is negative. Fig. 1a, b (left column) presents the RBs polarized in the **a**–**c** plane between 300 to 800 cm^{-1} in monoclinic crystal $CdWO_4$ and β-Ga_2O_3, respectively. If a pair of RBs is separated (overlapped) from each other, at the LO frequency of the first band, ω_{LO1}, the real part of ε_2 is positive (negative), as shown in the right panel of Fig. 1a, b. In previously reported materials, two adjacent RBs are either separated (Fig. 1a, $CdWO_4$) or overlapped (Fig. 1b, β-Ga_2O_3), leading to a hyperbolic-to-elliptic transition or vice versa in the momentum space when tuning the working frequency. Under the condition of separated RBs, the hyperbolic response with tunable TA is limited within a specific RB; with overlapping RBs, such spectral range is rather narrow as the in-plane hyperbolic response can only exist within the non-overlapped region. Therefore, the frequency range of hyperbolic polaritons with regulable propagation direction is confined within a specific RB, hindering their applications over a broad bandwidth.

In this paper, we report the hyperbolic-to-hyperbolic transition in a rare-earth oxyorthosilicate Y_2SiO_5 at a ERP, where two neighboring RBs almost kiss each other. Such an attribute breaks the limitation that the successive modulation of the propagation direction can only be realized within a single RB and makes it possible to achieve accurate nano-light control across multiple RBs. We directly observe the clapping process during the topological transition using scattering-type scanning near-field optical microscopy (s-SNOM). Along with the rotating TA, the hyperbolic branches close gradually and reopen again in the nearby RB. We theoretically explain that such evolution is mainly due to the interplay between two adjacent RBs. Furthermore, we indicate that even if there is only one single RB, the TA can still rotate dynamically under the influence of the high-frequency permittivity tensor. Our direct observation of this peculiar transformation of hyperbolic surface modes deepens the understanding of the PhPs in LSCs and affords possibilities for precise and spectrally robust modulation of the polariton behavior at the interface.

Results

Dispersive polaritons in monoclinic crystal Y_2SiO_5

Due to their distinctive characteristics, rare-earth oxyorthosilicates are suitable for a wide range of applications such as scintillator material, active laser medium, and so on. For example, monoclinic crystal Y_2SiO_5 has been widely used in many optical applications such as x-ray detection[41], electromagnetically induced transparency[42], and laser devices[43,44]. Its crystal structure is shown in Fig. 2a with **b** perpendicular to the **a**–**c** plane and the monoclinic angle $\beta = 102.45°$[45]. Viewing along the **b**-axis, Cartesian coordinate **xyz** can be defined to better describe its optical anisotropic properties[46]. The non-vertical relationship between the **a** and **c**-axis makes its symmetry lower than orthorhombic crystals, leading to in-plane phonon modes along various directions. In the Y_2SiO_5 crystal within the range from 40 to 1200 cm^{-1}, 23 phonon modes oscillate along the **b** vector, showing A_u symmetry; 22 phonon modes oscillate in the **a**–**c** plane with different orientations, presenting B_u symmetry[45]. The left panel in Fig. 1c demonstrates its RBs with B_u symmetry from 350 to 1050 cm^{-1}, with 2 ERPs marked by dashed blue lines. At ERPs, two adjacent RBs almost touch each other, resulting in $\mathrm{Re}(\varepsilon_2) \approx 0$ at ω_{LO1} (Fig. 1c, right column). Due to the limitation of laser source, here we focus on ERP1 at mid-infrared range between RB 11 (mode A) and RB 12 (mode B). Fig. 2b schematically shows two optical phonon modes under our investigation, with the orientation of the displacement vectors relative to the **x**-axis as 19.2° (OA) and 95.07° (OB) for modes A and B, respectively. For optical phonon mode A (blue arrow in Fig. 2b), its RB is bounded between the TO and LO frequencies as 902 cm^{-1} to 972 cm^{-1}, while the RB of mode B (red arrow in Fig. 2b) starts from 970 cm^{-1} and ends at 1050 cm^{-1} [45].

To directly visualize the evolution of polaritons, we perform direct nanoimaging of the (010) crystal surface using s-SNOM. Here, gold nanodisks with ~1 μm diameter are deposited to excite the polaritons at the Y_2SiO_5 crystal-air interface (see "Methods"). By scanning the sample surface point by point, direct nanoimaging of the surface polaritons can be obtained. It should be noticed that the *p*-polarized laser beam is illuminating along the **x**-axis defined in Fig. 2a with an incident angle relative to the surface as 30°. The real-space nanoimaging of PhPs in mode A is shown in Fig. 2c–f. Even though with a spherical edge shape where the gold antenna can support polaritons propagating along all directions, we can only observe highly directional polaritons at the crystal-air interface, unveiling the remarkably confined property and hyperbolic dispersion contours of the Y_2SiO_5 crystal. Accordingly, the Fourier spectrum can be calculated by applying Fourier transformation to the optical signals, further verifying the hyperbolic dispersion supporting high-**k** surface modes (Fig. 2g–j). With the laser frequency increasing, we can observe: (1) the open angle of the hyperbolic dispersion is decreasing, and the hyperbolic branches gradually close, which can be explained by the dispersive value of $-\mathrm{Re}(\varepsilon_2)/\mathrm{Re}(\varepsilon_1)$; (2) the angle between TA and the **x**-axis decreases gradually, mainly due to the influence of mode B and the interplay between these two RBs (see Supplementary Fig. 9).

The experimental results are further confirmed by full-wave simulations. Fig. 2k–n indicates the Fourier spectrum of the electric fields $\mathrm{Re}(E_z)$ 80 nm above the Y_2SiO_5 crystal surface excited by a **z**-oriented dipole source (see "Methods"). The distribution verifies the two observations we discussed above. When the frequency is increased, the TA, denoted by the green arrow, will rotate far away from the resonant direction of mode A (OA) and approach the vertical direction of mode B ($OB_\perp$). White curves indicate the iso-intensity contours (the points on the curve have the same intensity of the mode distribution) and the unequal lengths (the length between the original point and the furthest point of the iso-intensity contour of each petal) of the neighboring branches present the unbalanced shear response in the LSCs.

Next, we investigate the properties of PhPs of mode B. Here, we focus on the PhPs ranging from 970 cm^{-1} to 985 cm^{-1}. Fig. 3a–d shows the measured near-field signal at 970, 975, 979, and 981 cm^{-1}, respectively. The polaritons within this RB present shorter propagation lengths with increasing frequency. The corresponding dispersion in **k**-space is shown in Fig. 3e–h, indicating the gradual change of both TA and open angle. Corresponding simulation results of the Fourier

https://doi.org/10.1038/s41467-024-50939-0

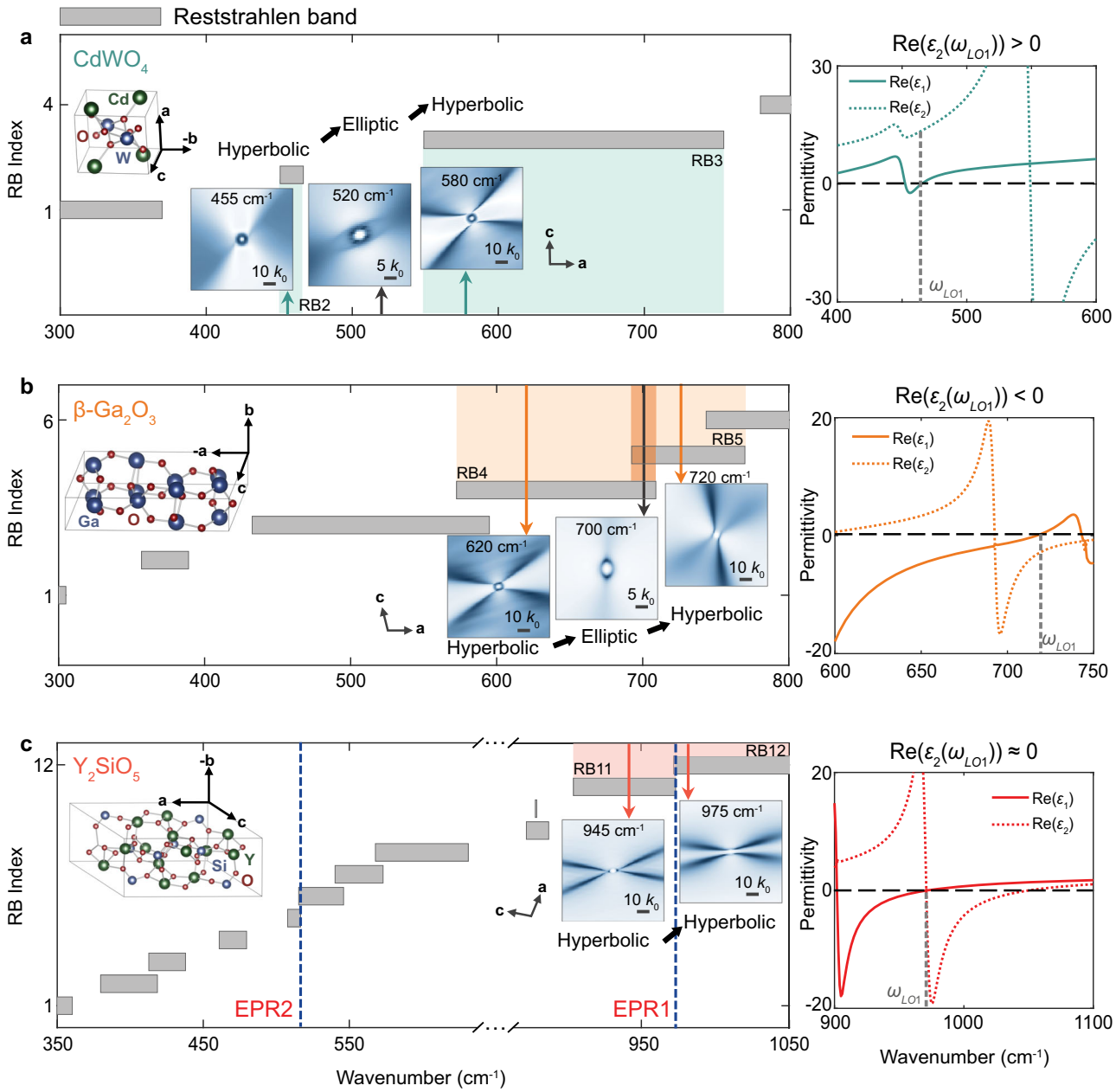

Fig. 1 | Comparison of Reststrahlen bands (RBs) in different low-symmetry crystals (LSCs). a the RBs in $CdWO_4$. The two RBs in green shade are separated in the spectrum, presenting an elliptic-like topology in the spectral gap. At the longitudinal optic (LO) frequency of the first RB in the green shade (RB2), the real part of the permittivity along the vertical direction is positive, indicating the separated features of these two RBs. **b** the RBs in β-Ga_2O_3. The two RBs in orange shade are overlapped in the spectrum, presenting an elliptic-like topology in the overlying region. At the LO frequency of the first RB in the orange shade (RB4), the real part of the permittivity along the vertical direction is negative, indicating overlapped features of these two RBs. **c** the RBs in Y_2SiO_5. The two RBs in the red shade just touch each other in the spectrum at the exceptional Reststrahlen point (ERP), presenting a hyperbolic-to-hyperbolic transition in the reciprocal space. At the LO frequency of the first RB in the red shade (RB11), the real part of the permittivity along the vertical direction is around zero, indicating the kissing features of these two RBs. The insets in the left column demonstrate the Fourier spectrums obtained by numerical simulations through a dipole source. The **z**-oriented dipole is placed 100 nm above the crystal surface. The subfigures in the right column show the real part of permittivity along two perpendicular directions.

spectrum are demonstrated in Fig. 3i–l, further verifying the rotational TA and varying open angle. This peculiar phenomenon has not been reported in the previous studies on PhPs in higher-symmetry crystals such as hBN, α-MoO_3, and calcite due to their higher symmetry and perpendicular (or parallel) phonon resonances.

Evolution of polaritons and hyperbolic-to-hyperbolic transition at ERP

To comprehensively understand the physics behind the dynamic change near the ERP, we investigate such a phenomenon from a theoretical aspect. Considering each phonon mode as an anharmonic broadened Lorentzian oscillator (see "Methods"), the dielectric response is the combined effect of all the resonances, where modes with A_u symmetry contribute to out-of-plane responses along the **b**-axis and B_u symmetry lead to responses in the **a**–**c** plane. For each phonon mode with B_u symmetry, we define the angle between its oscillation orientation and **a** vector as σ_m (m ranges from 1 to 22 for all modes with B_u symmetry), which are all different from each other (see Supplementary Table 1 and Supplementary Fig. 1). In monoclinic crystals, the dielectric tensor is determined by four independent

https://doi.org/10.1038/s41467-024-50939-0

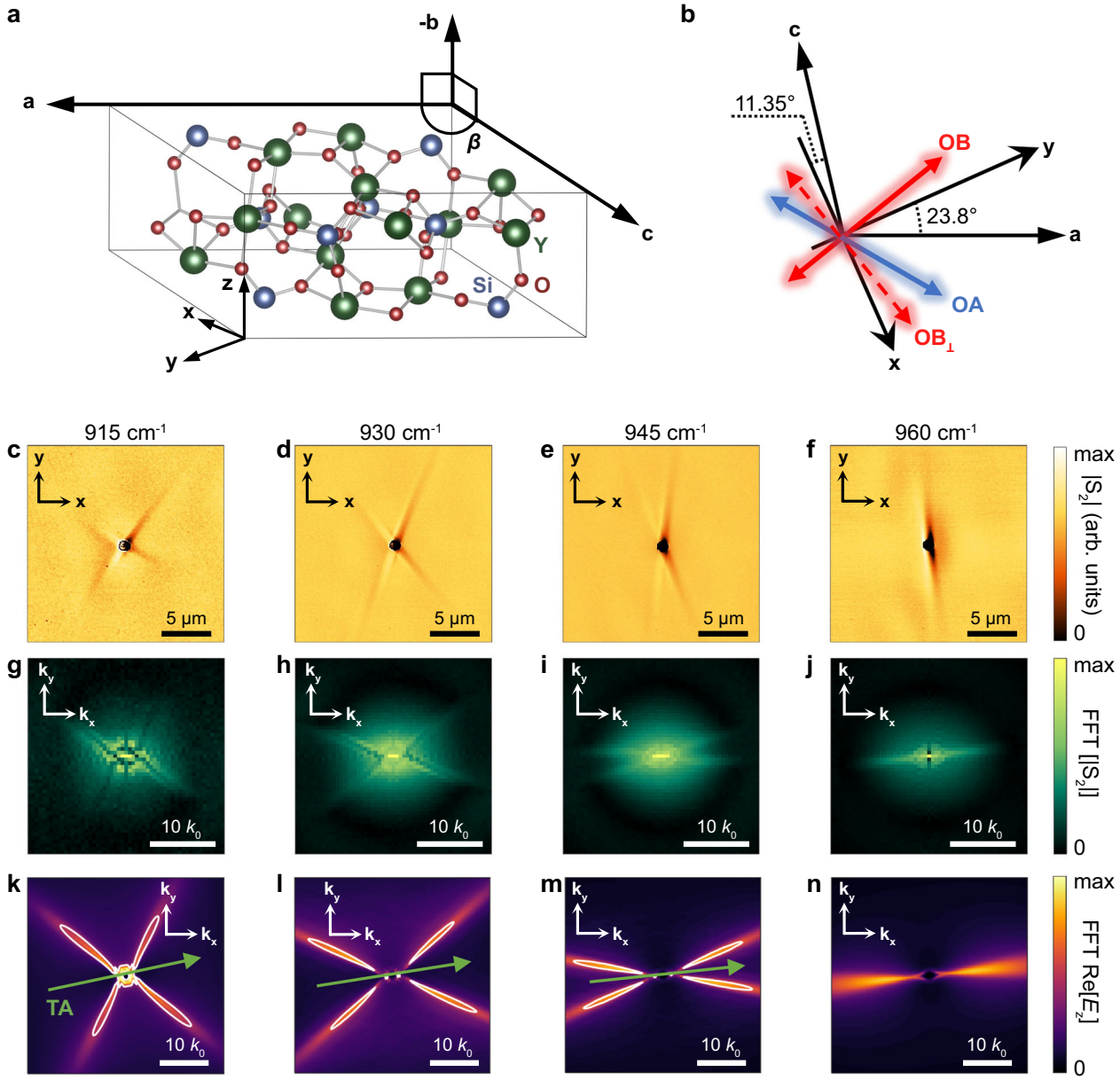

Fig. 2 | Evolution of the dispersive polaritons in phonon mode A in monoclinic crystal Y_2SiO_5. **a** the crystal structure of monoclinic crystal Y_2SiO_5. Vector **b** is perpendicular to the **a**–**c** plane, with the monoclinic angle β between **a** and **c** equal to 102.45°. **b** Cartesian coordinate **xyz** is defined to describe the optical properties in this work. Optical phonon modes A and B are the two non-perpendicular modes under our investigation. OA and OB indicate the direction of phonon modes A and B, respectively. $OB_\perp$ indicates the vertical direction of phonon mode B. **c**–**f** the measured near-field signal $|S_2|$ with different incident frequencies using scattering-type scanning near-field optical microscopy (s-SNOM). The phonon polaritons (PhPs) are launched by an Au nanodisk antenna with a diameter of ~1 μm and thickness of 100 nm. The incident laser beam is aligned with the **x**-axis with *p*-polarization. **g**–**j** corresponding Fourier spectrum of the panel (**c**–**f**) obtained by calculating their Fourier transformation, justifying the hyperbolic dispersion of the PhPs. **k**–**n** the Fourier spectrum of dipole-launched polaritons through numerical simulations. The **z**-oriented dipole is placed 100 nm above the crystal surface. The green arrows indicate the transverse axis (TA) at different frequencies, which is rotating to approach $OB_\perp$ with increasing frequency. White curves indicate the iso-intensity contours (the points on the curve have the same intensity of the mode distribution) and the unequal lengths (the length between the original point and the furthest point of the iso-intensity contour of each petal) of the neighboring branches present the unbalanced shear response in the LSC.

components as

$$\bar{\bar{\varepsilon}}(f)=\begin{bmatrix}\varepsilon_{xx}(f) & \varepsilon_{xy}(f) & 0\\ \varepsilon_{yx}(f) & \varepsilon_{yy}(f) & 0\\ 0 & 0 & \varepsilon_{zz}(f)\end{bmatrix} \quad (1)$$

where ε_{xy} equals to ε_{yx} as shear elements. Each component in the permittivity tensor is a complex value, which varies with optical frequency. Due to the existence of the off-diagonal terms in $\bar{\bar{\varepsilon}}(f)$, the TA of the hyperbolic dispersion curve is neither aligned to the **x** nor **y**-axis. If we ignore the imaginary part and apply rotation matrix $R(\theta)$ to diagonalize the real part of the permittivity tensor, the direction of the TA could be determined. Simultaneously, the non-diagonalizable imaginary part of the permittivity tensor contributes to the recently reported shear phenomenon[32]. The θ value at a specific frequency is affected by the combined effects of all the non-parallel modes in the **a**–**c** plane as well as the high-frequency components of the permittivity tensor. In this paper, the rotational TA is mainly because of the

https://doi.org/10.1038/s41467-024-50939-0

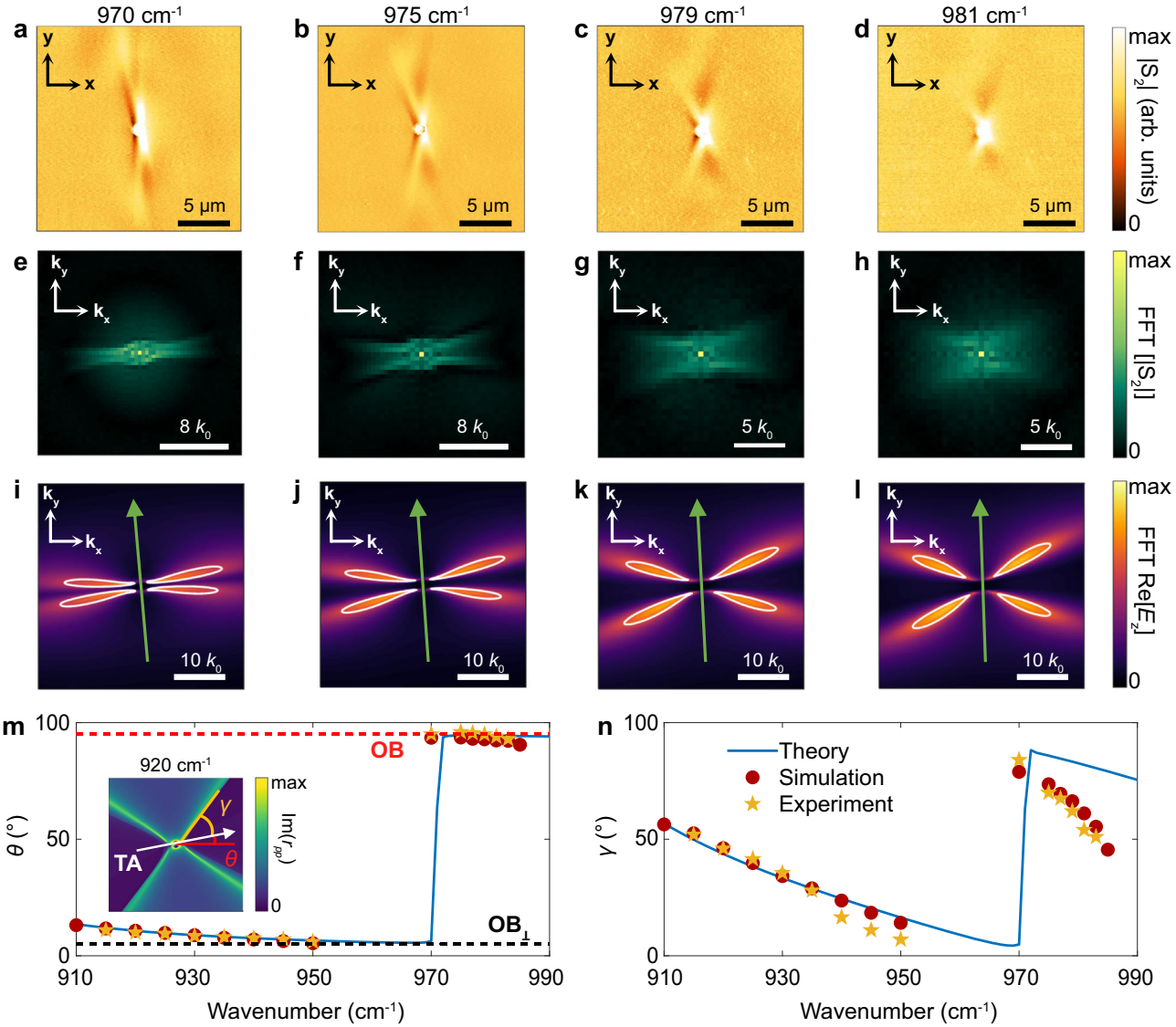

Fig. 3 | Evolution of the dispersive polaritons at ERP1 in monoclinic crystal Y_2SiO_5. a–d the measured near-field signal $|S_2|$ with different incident frequencies using s-SNOM. The PhPs are launched by an Au nanodisk antenna with a diameter of ~1 μm and thickness of 100 nm. The incident laser beam is aligned with the **x**-axis with *p*-polarization. **e–h** corresponding Fourier spectrum of the panel (**a–d**) obtained by calculating their Fourier transformation. **i–l** the Fourier spectrum of dipole-launched polaritons through numerical simulations. The **z**-oriented dipole is placed 100 nm above the crystal surface. The green arrows indicate the TA at different frequencies, which is moving far away from OB with increasing frequency. White curves indicate the iso-intensity contours (the points on the curve have the same intensity of the mode distribution) and the unequal lengths (the length between the original point and the furthest point of the iso-intensity contour of each petal) of the neighboring branches present the unbalanced shear response in the LSC. **m** the evolution of θ and **n** open angle γ versus frequency near ERP1. As indicated in the inset, θ is defined as the angle between TA and the **x**-axis. The values of θ and γ both have a 90-degree step change at ERP1. Blue solid curve: calculated theoretical results by $\tan^{-1}[-\mathrm{Re}(\varepsilon_2)/\mathrm{Re}(\varepsilon_1)]$; red dots: simulation results obtained from the dipole launched polaritons using the finite-element method same as panel (**i–l**) (see "Methods"); yellow pentacles: experimental results obtained by measuring the near-field optical signals under the excitations of different frequencies using s-SNOM (see "Methods"). Inset in panel (**m**) the analytically calculated imaginary part of the reflection coefficient at 920 cm^{-1}.

interplay between the two non-orthogonal phonon modes A and B with B_u symmetry oscillating in the **a–c** plane (see Supplementary Fig. 9).

TA and open angle are two determinant parameters for a hyperbolic dispersion, as the shape of the IFC can be decided after these two values are found. To comprehensively analyze the evolution of polaritons at the ERP, here we denote the open angle as γ and the angle between TA and the **x**-axis as θ (inset of Fig. 3m). As we discussed above, the theoretical value of the TA can be calculated by finding the angle θ to diagonalize the real part of the permittivity tensor, leaving the off-diagonal term as a pure imaginary value (see Supplementary Fig. 2). Then, the open angle γ can be obtained by $\tan^{-1}[-\mathrm{Re}(\varepsilon_2)/\mathrm{Re}(\varepsilon_1)]$, where ε_1 and ε_2 are the permittivity along the direction of TA and the direction perpendicular to it, respectively. In addition, the electrical field and the corresponding dispersion in **k**-space can be obtained by numerically simulating the dipole-launched polaritons at the crystal-air interface, from which the simulation results of TA and open angle can be directly measured (see "Methods"). As shown in Fig. 3m, when the working frequency is increased from the resonant frequency of mode A, θ will decrease and approach the vertical direction of mode B ($OB_\perp$). At the ERP, where the two bands just touch each other, θ jumps 90 degrees from $OB_\perp$ to OB. Then, TA deviates from the orientation of mode B when moving far away from its resonant frequency. Moreover, the open angle γ drops when we increase the optical frequency with a span of ~40° from 915 cm^{-1} to 955 cm^{-1}. Near the ERP, a 90-degree step change happens, followed by a similar decrease of γ value in mode A,

which is caused by the spectrally dispersive ε_1 and ε_2 (Fig. 3n). In short, the dispersion of PhPs experiences a clapping process: the hyperbola closes with increasing frequency and reopens after the ERP with rotatory TA. Moreover, the rotation of TA can be expected: when the working frequency is approaching the oscillation frequency of the nearby mode, the TA will also rotate to approach the vertical direction of the adjacent phonon mode.

Effect of high-frequency permittivity on TA rotation

As claimed before, the dynamic rotation of TA is mainly due to the interplay of the two touching RBs. Because of the non-perpendicular polarized directions, the oscillations of these two phonon modes have mutual effects on each other. Nevertheless, we declare that even with the existence of only one RB, the TA can also dynamically rotate when tuning the working frequency (Fig. 4a), which is because the anisotropy and orientation of high-frequency permittivity also affect TA. Fig. 4b demonstrates the dispersion of polaritons in material $\varepsilon_{XY} = \begin{pmatrix} 1.75 & -0.433 \\ -0.433 & 1.25 \end{pmatrix}$ with $k_z = 0$, which can be diagonalized to $\varepsilon_{12} = \begin{pmatrix} 2 & 0 \\ 0 & 1 \end{pmatrix}$ with $\alpha = 60°$.

Next, we investigate how the anisotropy (φ) and orientation (α) affect the TA rotation in the single-RB case. To simplify the problem, we only consider the oscillation of mode A with $\theta = 19.2°$ and high-frequency terms in permittivity tensor. Firstly, we set $\varepsilon_{xy\infty} = 0$ and fix the determinant of ε_{XY}. By changing the angle φ, we could modulate the anisotropy of the elliptical dispersion. As shown in Fig. 4c, the adjustment of φ can lead to different evolutions of TA. When $\varphi = 0°$, the dispersion relation is shaped as a straight line along the **x**-axis, and θ decreases gradually. By slightly increasing φ, the dispersion curve will evolve into an ellipse with a long axis along the **x** direction, accompanied by a slower decline of θ value. When $\varphi = 45°$, the dispersion will become spherical shape with no anisotropy, and the TA will stay fixed as $\theta = 19.2°$, no matter how the working frequency changes. With φ further increasing, the long axis of the ellipse is along the **y**-axis. Under this condition, θ increases with optical frequency, and the growth rate is faster with a larger φ value. Based on these observations, we could draw two conclusions: (1) TA stays fixed with isotropic high-frequency permittivity; (2) TA rotates to approach the long axis of the dispersion curve as the working frequency moves far away from the oscillation frequency with changing rate positively correlated with the anisotropy.

Then, we fix the anisotropy and analyze the relationship between the TA and α. The value of φ is set as $\tan\varphi = 2$ with long axis along **x** direction with $\alpha = 0°$. From Fig. 4d, it can be observed that the angle of the long axis can drastically affect the TA rotation. When $\alpha = 0°$, θ value decreases gradually and approaches the **x**-axis with increasing frequency. With α increasing slightly, the TA instead rotates anticlockwise to approach the long axis of the ellipse. It could be noticed that when $\alpha = 90°$ the growth rate of θ value is slower than that under the condition of $\alpha = 60°$. By further lifting the α value, the TA surprisingly decreases gradually. This phenomenon is further discussed in detail in the Supplementary Note 5. It shows that the TA rotates to approach the long axis of the ellipse and stays fixed when any symmetrical axis of the ellipse (either the major axis or the minor axis) is aligned to the polarization direction of the phonon mode.

Discussion

The results presented here show a hyperbolic-to-hyperbolic transition in LSCs, which is in contrast to the hyperbolic (elliptic)-to-elliptic

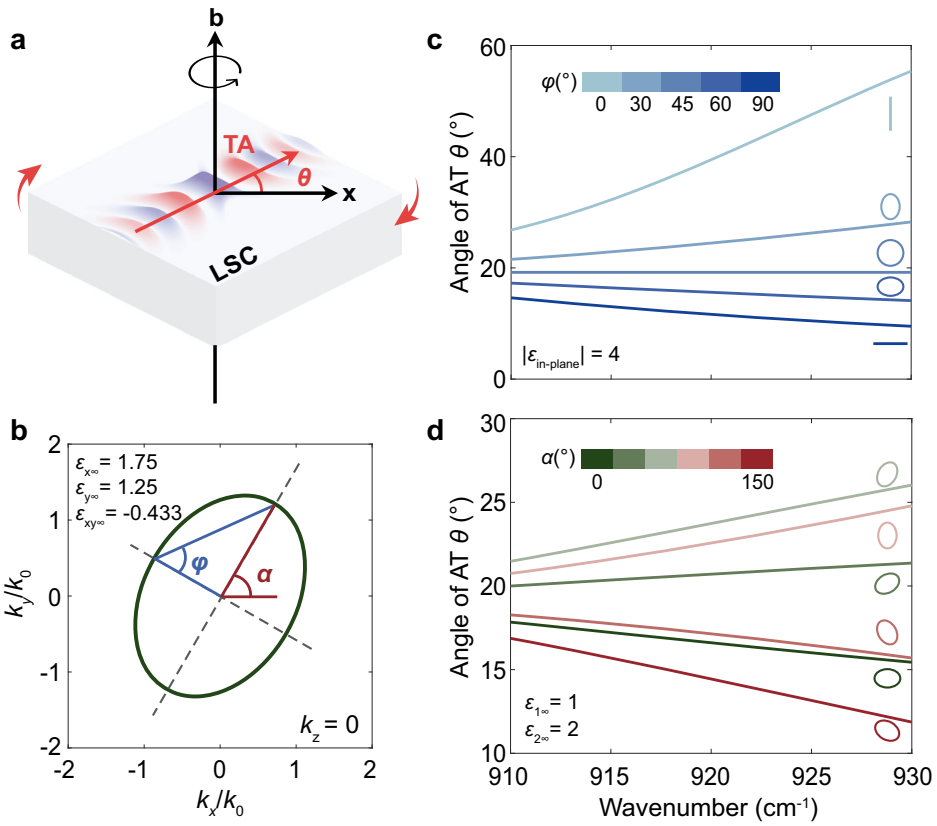

Fig. 4 | The TA rotation in crystals with the existence of only a single RB. a the schematic diagram showing the rotation of TA in LSCs with a single-RB case under the effect of high-frequency permittivity. **b** the in-plane dispersion when only considering the anisotropic high-frequency permittivity at $k_z = 0$. α represents the angle between $\mathbf{k_x}$-axis and the long axis of the ellipse. $\tan\varphi$ represents the ratio between the lengths of the ellipse along two symmetrical axes. **c** the rotation of TA with different φ values and fixed determinants of high-frequency permittivity. The $\varepsilon_{xy\infty}$ is set as zero. **d** the rotation of TA with different α values and fixed anisotropy.

(hyperbolic) transition in previously reported materials. Such hyperbolic-to-hyperbolic transition happens where the two adjacent RBs almost kiss each other, accompanied by dispersive open angle and TA. These phenomena are mainly attributed to the mutual effect of two adjacent non-orthogonal modes, which is prohibited in high-symmetry crystals such as α-MoO_3 and hBN. The evolution of the TA can be predicted: it gradually deviates from the resonance orientation and approaches the vertical direction of the adjacent mode when the operation frequency moves far away from the resonant frequency of the first mode and close to the nearby RB. Moreover, we find that even with the existence of only one RB in the optical crystal, the TA can also be rotational under the effect of anisotropic high-frequency permittivity. Furthermore, as the displacements in phonon modes are mainly ascribed to the motions of oxygen and silicon atoms, isostructural rare-earth oxyorthosilicates, such as Lu_2SiO_5, can also have similar phonon mode behavior and polariton properties (see Supplementary Figs. 14, 15)[47]. Therefore, as a prospective playground for light manipulation at the nanoscale, we anticipate more rare-earth oxyorthosilicates to be explored and applied for nano-device design in the future.

In summary, we study the ERP where the two adjacent RBs almost touch each other in monoclinic Y_2SiO_5 crystal. The hyperbolic-to-hyperbolic transition is observed when moving the working frequency across the ERP, accompanied by a 90-degree step change of both open angle and TA, which are dispersive in each single RB. These findings deepen the understanding of PhPs in LSCs and enrich the material library for light control at the nanoscale. The continuously rotated TA gives the opportunity for spectrally robust and precise control of the nano-light and energy flow.

Methods

Analytical model for Y_2SiO_5 permittivity tensor

Each optical phonon can be modeled as an anharmonic broadened Lorentzian oscillator as

$$\eta_m(\omega) = \frac{A_m^2 - i\omega\Gamma_m}{\omega_{TO,m}^2 - \omega^2 - i\omega Q_m}. \tag{2}$$

Here, A_m, Γ_m, $\omega_{To,m}$, and Q_m represent the amplitude, anharmonic broadening parameter, resonance frequency for TO modes, and harmonic broadening parameter, respectively. Then, the permittivity tensor can be written as Eq. (1) with the combined effect of 22 optical phonons with B_u symmetry and 23 optical phonons with A_u symmetry. Thus, we can obtain

$$\varepsilon_{xx} = \varepsilon_{\infty,xx} + \sum_{m=1}^{22} \eta_m^{B_u} \cos^2\rho_m, \tag{3a}$$

$$\varepsilon_{xy} = \varepsilon_{\infty,xy} + \sum_{m=1}^{22} \eta_m^{B_u} \sin\rho_m \cos\rho_m, \tag{3b}$$

$$\varepsilon_{yy} = \varepsilon_{\infty,yy} + \sum_{m=1}^{22} \eta_m^{B_u} \sin^2\rho_m, \tag{3c}$$

$$\varepsilon_{zz} = \varepsilon_{\infty,zz} + \sum_{i=1}^{23} \eta_i^{A_u} \tag{3d}$$

In equation (3) ρ_m denotes the relative angle between the orientation of the m^{th} phonon mode and the **x**-axis, which are all different from each other. And ε_∞ is the high-frequency permittivity of each component, which is given by $\varepsilon_{\infty,xx} = 3.166$, $\varepsilon_{\infty,xy} = 0.0027$, $\varepsilon_{\infty,yy} = 3.127$, and $\varepsilon_{\infty,zz} = 3.114$.

Sample fabrication

The crystal was polished at the (010) surface with a size of 10 mm × 10 mm × 1 mm, which is much larger than the operating frequency of the PhPs. Photoresist (PMMA 495 A5) was first spin-coated on the sample surface, followed by 2-min baking at 180 °C. Then, a charge dissipating agent (ESPACER 300Z) was spin-coated with 2000 rpm of 70 seconds to form a highly conductive film on the surface. Then the pattern of Au nanodisks was printed using an electron beam lithographer (JBX-6300FS). Next, the sample was washed with deionized water to remove the conductive film. Then the sample was soaked in developing solution (MIBK: IPA = 1:3) for 30 seconds and soaked in IPA for 30 seconds to wash away the residual MIBK, followed by a 3 nm Ti/100 nm Au deposition using AJA E-beam evaporator. Finally, a standard lift-off procedure was performed.

Numerical simulations

Numerical simulations were performed using the finite-element method through commercial software COMSOL Multiphysics 5.5. A **z**-oriented dipole was placed 100 nm above the crystal surface in the air as a source. The electric field distribution was measured at 80 nm above the top surface to measure the surface mode at the crystal-air interface. The simulation region was set as 25 μm × 25 μm with scattering boundary conditions to prevent the reflected wave from the material edges. The image maps in the reciprocal space can be obtained by doing a 2D Fourier transformation of the field distributions in real space. The direction of the dispersion curve was determined by finding the point with maxima at each row and calculating the angle of their connecting lines.

s-SNOM measurements

The near-field optical signals were measured using commercial s-SNOM (Neaspec) at reflection mode. The infrared laser beam was focused by a parabolic mirror on the AFM tip. Supplementary Fig. 4 shows the schematic diagram of the experimental setup. The incident *p*-polarized light is illuminated on the sample aligned to the **x**-axis with an incident angle of 30° relative to the surface. During the measurement, the sample stage is moving and the AFM tip in the tapping mode can scan horizontally to obtain the amplitude of the second harmonic signal S_2. The measured area is 20 μm × 20 μm.

Data availability

The data supporting the findings of this work are available within the paper and its supplementary information. All raw data of this work is available from the corresponding authors upon request.

References

1. Lee, D. et al. Hyperbolic metamaterials: fusing artificial structures to natural 2D materials. *eLight* **2**, 1 (2022).
2. Guo, Z., Jiang, H. & Chen, H. Hyperbolic metamaterials: From. *J. Appl. Phys.* **127**, 071101 (2020).
3. Huo, P., Zhang, S., Liang, Y., Lu, Y. & Xu, T. Hyperbolic metamaterials and metasurfaces: Fundamentals and applications. *Adv. Opt. Mater.* **7**, 1801616 (2019).
4. Poddubny, A., Iorsh, I., Belov, P. & Kivshar, Y. Hyperbolic metamaterials. *Nat. Photonics* **7**, 948–957 (2013).
5. Low, T. et al. Polaritons in layered two-dimensional materials. *Nat. Mater.* **16**, 182–194 (2017).
6. Krishnamoorthy, H. N., Jacob, Z., Narimanov, E., Kretzschmar, I. & Menon, V. M. Topological transitions in metamaterials. *Science* **336**, 205–209 (2012).
7. Liu, Z., Lee, H., Xiong, Y., Sun, C. & Zhang, X. Far-field optical hyperlens magnifying sub-diffraction-limited objects. *Science* **315**, 1686–1686 (2007).
8. Tumkur, T. et al. Control of spontaneous emission in a volume of functionalized hyperbolic metamaterial. *Appl. Phys. Lett.* **99**, 151115 (2011).

9. Rho, J. et al. Spherical hyperlens for two-dimensional sub-diffractional imaging at visible frequencies. *Nat. Commun.* **1**, 143 (2010).
10. Kruk, S. S., Powell, D. A., Minovich, A., Neshev, D. N. & Kivshar, Y. S. Spatial dispersion of multilayer fishnet metamaterials. *Opt. Express* **20**, 15100–15105 (2012).
11. Yin, S., Galiffi, E. & Alù, A. Floquet metamaterials. *eLight* **2**, 8 (2022).
12. Yang, X., Yao, J., Rho, J., Yin, X. & Zhang, X. Experimental realization of three-dimensional indefinite cavities at the nanoscale with anomalous scaling laws. *Nat. Photonics* **6**, 450–454 (2012).
13. Guo, P., Chang, R. P. H. & Schaller, R. D. Tunable infrared hyperbolic metamaterials with periodic indium-tin-oxide nanorods. *Appl. Phys. Lett.* **111**, 021108 (2017).
14. Vasilantonakis, N., Nasir, M. E., Dickson, W., Wurtz, G. A. & Zayats, A. V. Bulk plasmon-polaritons in hyperbolic nanorod metamaterial waveguides. *Laser Photonics Rev.* **9**, 345–353 (2015).
15. High, A. A. et al. Visible-frequency hyperbolic metasurface. *Nature* **522**, 192–196 (2015).
16. Gomez-Diaz, J. S., Tymchenko, M. & Alu, A. Hyperbolic plasmons and topological transitions over uniaxial metasurfaces. *Phys. Rev. Lett.* **114**, 233901 (2015).
17. Hu, G., Krasnok, A., Mazor, Y., Qiu, C. W. & Alu, A. Moire hyperbolic metasurfaces. *Nano Lett.* **20**, 3217–3224 (2020).
18. Hu, G., Zheng, C., Ni, J., Qiu, C.-W. & Alù, A. Enhanced light-matter interactions at photonic magic-angle topological transitions. *Appl. Phys. Lett.* **118**, 211101 (2021).
19. Li, P. et al. Infrared hyperbolic metasurface based on nanostructured van der Waals materials. *Science* **359**, 892–896 (2018).
20. Li, P. et al. Collective near-field coupling and nonlocal phenomena in infrared-phononic metasurfaces for nano-light canalization. *Nat. Commun.* **11**, 3663 (2020).
21. Caldwell, J. D. et al. Sub-diffractional volume-confined polaritons in the natural hyperbolic material hexagonal boron nitride. *Nat. Commun.* **5**, 5221 (2014).
22. Giles, A. J. et al. Ultralow-loss polaritons in isotopically pure boron nitride. *Nat. Mater.* **17**, 134–139 (2018).
23. Ma, W. et al. In-plane anisotropic and ultra-low-loss polaritons in a natural van der Waals crystal. *Nature* **562**, 557–562 (2018).
24. Hu, H. et al. Doping-driven topological polaritons in graphene/α-MoO_3 heterostructures. *Nat. Nanotechnol.* **17**, 940–046 (2022).
25. Zheng, Z. et al. A mid-infrared biaxial hyperbolic van der Waals crystal. *Sci. Adv.* **5**, eaav8690 (2019).
26. Taboada-Gutiérrez, J. et al. Broad spectral tuning of ultra-low-loss polaritons in a van der Waals crystal by intercalation. *Nat. Mater.* **19**, 964–968 (2020).
27. Correas-Serrano, D., Gomez-Diaz, J. S., Melcon, A. A. & Alù, A. Black phosphorus plasmonics: anisotropic elliptical propagation and nonlocality-induced canalization. *J. Opt.* **18**, 104006 (2016).
28. Zheng, C. et al. Molding broadband dispersion in twisted trilayer hyperbolic polaritonic surfaces. *ACS Nano* **16**, 13241–13250 (2022).
29. Wang, C. et al. Van der Waals thin films of WTe_2 for natural hyperbolic plasmonic surfaces. *Nat. Commun.* **11**, 1158 (2020).
30. Ma, W. et al. Ghost hyperbolic surface polaritons in bulk anisotropic crystals. *Nature* **596**, 362–366 (2021).
31. Hu, C. et al. Source-configured symmetry-broken hyperbolic polaritons. *eLight* **3**, 14 (2023).
32. Passler, N. C. et al. Hyperbolic shear polaritons in low-symmetry crystals. *Nature* **602**, 595–600 (2022).
33. Matson, J. et al. Controlling the propagation asymmetry of hyperbolic shear polaritons in beta-gallium oxide. *Nat. Commun.* **14**, 5240 (2023).
34. Hu, G. et al. Real-space nanoimaging of hyperbolic shear polaritons in a monoclinic crystal. *Nat. Nanotechnol.* **18**, 64–70 (2023).
35. Tielrooij, K.-J. et al. Out-of-plane heat transfer in van der Waals stacks through electron–hyperbolic phonon coupling. *Nat. Nanotechnol.* **13**, 41–46 (2018).
36. Hu, G. et al. Topological polaritons and photonic magic angles in twisted α-MoO_3 bilayers. *Nature* **582**, 209–213 (2020).
37. Zheng, Z. et al. Controlling and focusing in-plane hyperbolic phonon polaritons in α-MoO_3 with a curved plasmonic antenna. *Adv. Mater.* **34**, 2104164 (2022).
38. Qu, Y. et al. Tunable planar focusing based on hyperbolic phonon polaritons in α-MoO_3. *Adv. Mater.* **34**, 2105590 (2022).
39. Zhang, T., Zheng, C., Chen, Z. N. & Qiu, C.-W. Negative reflection and negative refraction in biaxial van der Waals materials. *Nano Lett.* **22**, 5607–5614 (2022).
40. Wang, M. et al. Spin-orbit-locked hyperbolic polariton vortices carrying reconfigurable topological charges. *eLight* **2**, 12 (2022).
41. Dhanaraj, G., Byrappa, K., Prasad, V. & Dudley, M. *Springer handbook of crystal growth*. Vol. 2 (Springer, 2010).
42. Li, Z., Liu, J., Yu, P. & Zhang, G. Birefringence and polarization rotator induced by electromagnetically induced transparency in rare earth ion-doped crystals. *Appl. Phys. B* **122**, 109 (2016).
43. Yen-Kuang, K., Man-Fang, H. & Birnbaum, M. Tunable Cr^{4+}:YSO Q-switched Cr:LiCAF laser. *IEEE J. Quantum Electron.* **31**, 657–663 (1995).
44. Deka, C. et al. Laser performance of Cr^{4+}:Y_2SiO_5. *Appl. Phys. Lett.* **61**, 2141–2143 (1992).
45. Mock, A., Korlacki, R., Knight, S. & Schubert, M. Anisotropy and phonon modes from analysis of the dielectric function tensor and the inverse dielectric function tensor of monoclinic yttrium orthosilicate. *Phys. Rev. B* **97**, 165203 (2018).
46. Li, C., Wyon, C. & Moncorge, R. Spectroscopic properties and fluorescence dynamics of Er^{3+} and Yb^{3+} in Y_2SiO_5. *IEEE J. Quantum Electron.* **28**, 1209–1221 (1992).
47. Stokey, M. et al. Infrared active phonons in monoclinic lutetium oxyorthosilicate. *J. Appl. Phys.* **127**, 115702 (2020).

Acknowledgements

C.-W.Q. acknowledges financial support from the National Research Foundation, Prime Minister's Office, Singapore, under Competitive Research Program Award NRF-CRP26-2021-0004. C.-W.Q. is also supported by a grant (A-0005947-16-00) from the Advanced Research and Technology Innovation Center (ARTIC) at the National University of Singapore. Q.W. is supported by the Agency for Science, Technology, and Research (A*STAR) under AME IRG Grant No. A20E5c0095, Career Development Fund Grant No. C210112044. G.H. acknowledges the Nanyang Assistant Professorship Start-up Grant, Ministry of Education (Singapore) under AcRF TIER1(RG61/23), and the National Research Foundation of Singapore under award no. CRP22-2019-0064. X.M. acknowledges the Agency for Science, Technology and Research (A*STAR) under the Career Development Fund-Seed Projects 222D800038, and MTC Young Individual Research Grants (YIRG) M23M7c0129. The authors thank Dr. Qiangbing Guo (National University of Singapore) and Dr. Xianghong Kong (National University of Singapore) for helpful discussions.

Author contributions

C.-W.Q. conceived the idea and supervised the project overall. C.Z. and G.H. conducted the theoretical analysis and numerical simulations. C.Z. and J.W. fabricated the samples with the help of Y.C. C.Z. performed the near-field measurement with significant input from Q.W., X.M, and Z.L. G.H., C.-W.Q., and C.Z. analyzed the experimental data with input from Q.W., P.L., and Z.N. C.Z. wrote the manuscript with the help of all the other authors. All the authors contribute significantly to the work.

Competing interests

The authors declare no competing of interests.

Additional information

Supplementary information The online version contains supplementary material available at https://doi.org/10.1038/s41467-024-50939-0.

Correspondence and requests for materials should be addressed to Qian Wang or Cheng-Wei Qiu.

Peer review information *Nature Communications* thanks the anonymous reviewer(s) for their contribution to the peer review of this work. A peer review file is available.